ACS APPLIED MATERIALS & INTERFACES

Research Article

www.acsami.org

Novel Morphology-Controlled Hierarchical Core@Shell Structural Organo-Layered Double Hydroxides Magnetic Nanovehicles for Drug Release

Xue Bi, Ting Fan, and Hui Zhang*

The State Key Laboratory of Chemical Resource Engineering, Beijing University of Chemical Technology, P.O. Box 98, Beijing 100029, China

Supporting Information

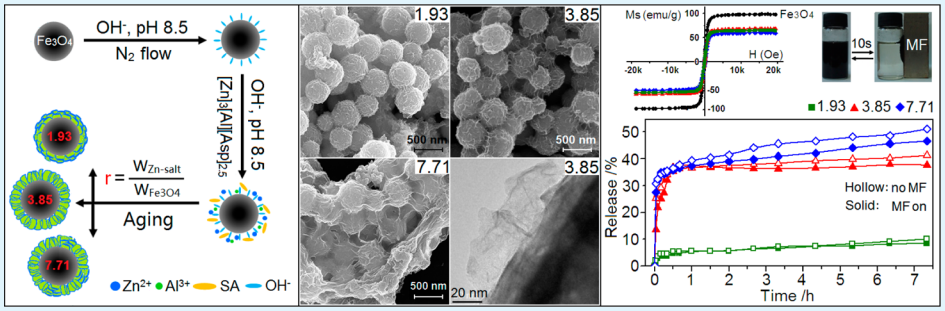

ABSTRACT: Novel hierarchical core@shell structured salicylate (SA) intercalated ZnAl-LDH (layered double hydroxides) magnetic nanovehicles were obtained via a special double-drop coprecipitation strategy assembling organo-ZnAl-LDH nanocrystals onto the surface of Fe_3O_4 submicrospheres (~480 nm) from cheap aspirin and Zn- and Al-nitrates in alkaline solutions. The obtained Fe_3O_4@SA-LDH-*r* nanovehicles exhibit varied morphologies with hexagonal LDH *ab*-face horizontal, vertical, and vertical/slant/horizontal to the surfaces of Fe_3O_4 upon proper mass ratio (*r*) of Zn-salt to Fe_3O_4 from 1.93 to 7.71 in a low supersaturation system and possess moderate drug loadings and strong superparamagnetism. An *in vitro* release study reveals that under "no MF" mode (without external magnetic field) the SA release exhibits the higher accumulated release amount and smaller half-life ($t_{0.5}$) for Fe_3O_4@SA-LDH-3.85 (41.2%, 1.63 min) and Fe_3O_4@SA-LDH-7.71 (51.1%, 1.66 min) probably owing to their mainly vertical LDH orientations, while the dramatically reduced SA release (10.0%) and greatly elongated $t_{0.5}$ (25.6 min) for Fe_3O_4@SA-LDH-1.93 may be due to its relatively stronger host−guest interaction and compact horizontally oriented LDH shell stack. Under "MF on" mode, all the magnetic samples show a detectable reduced SA release owing to the particle−particle interactions among the magnetic nanovehicles. The kinetic fittings show that the release processes of all the samples involve the bulk and surface diffusion. The SA release from Fe_3O_4@SA-LDH-1.93 is mainly determined by the interparticle diffusion among the horizontally oriented LDH shell nanocrystals while those of Fe_3O_4@SA-LDH-3.85 and Fe_3O_4@SA-LDH-7.71 mainly involve the interlayer intraparticle diffusion between LDHs layers due to their largely vertical LDH shell nanocrystals.

KEYWORDS: *organo-layered double hydroxides, salicylate, hierarchical core@shell structure, vertically oriented growth, superparamagnetism, in vitro drug release*

1. INTRODUCTION

Layered double hydroxides (LDHs), so-called hydrotalcite-like anionic clay, with a general formula of $[M^{2+}_{1-x}M^{3+}_{x}(OH)_2]^{x+}A^{n-}_{x/n}\cdot mH_2O$,[1,2] are widely used in catalysis,[3] environmental protection,[4,5] and biomedicine[6−9] due to their eminently ordered lamellar structure[2] and outstanding biocompatibility with low toxicity.[7,8,10] As a promising drug vehicle candidate, its principal application studies involve the sustained release of cardiovascular,[11] anti-inflammatory,[12] and anticancer drugs[13] but lack of adjustable targeted delivery ability. Fortunately, the magnetic nanoparticles as the next generation of the drug delivery system significantly facilitate the accurate transfer of drug molecules to the nidus with no side effects on the human body,[14] and their magnetic properties like superparamagnetism make the transportation of pharmaceuticals much more efficient.[15] So far, the classic core@shell model has been adopted by lots of magnetic drug-loading nanovehicles,[16] such as CD(cyclodextrin)-functionalized superparamagnetic iron oxide nanoparticles[17] or Fe_3O_4@SiO_2,[18,19] greatly improving the practical value of drug-loading nanovehicles. However, the study on assembling LDHs on the surface of magnetic particles as drug vehicles is far less

Received: September 8, 2014
Accepted: October 23, 2014
Published: October 23, 2014

than that of magnetic SiO_2. The controllable assembly of magnetically functionalized LDHs nanovehicles is still a challenge.

The first magnetic organo-LDH nanohybrid involving 5-aminosalicylate intercalated ZnAl-LDH and $MgFe_2O_4$ (~19 nm) via a conventional varied pH coprecipitation step (also called a single-drop method) was reported by Zhang et al. and proved to be a plausible core@shell structure with severely aggregated LDH nanoplates.[20] Carja et al.[21] applied the conventional constant pH coprecipitation route to prepare a new aspirin-LDH clay nanohybrid using FeO_x/Fe-LDH as a magnetic core showing coexistence of small Fe-oxide nanoparticles and fibrous drug particles on the surface of partially aggregated clay-like particles. The successive work of Zhang et al. on magnetic LDH nanohybrids containing ibuprofen[22] and diclofenac[23] by the single-drop method revealed a well-defined core@shell structure with compact drug-LDH shell nanoparticles, possessing quite small Scherrer dimensions, D_{110} (~14 nm), but cannot be distinguished from each other by TEM, over the surface of $MgFe_2O_4$ (~50 nm). Differently, the coprecipitation−calcination−reconstruction method renders such magnetic nanohybrids a loosely packed LDH shell with anticancer agent DFUR intercalated MgAl-LDH nanoplates (clearly observed by TEM as ~22 nm) parallel to the surface of larger Fe_3O_4 (~220 nm).[24] Ay et al.[25] reported the synthesis of magnetic salicylate-MgAl-LDH nanocomposites by ion exchange from a magnetic NO_3-LDH showing nearly spherical core−shell morphology with very small LDH nanoparticles on spherical ferrite cores (15−50 nm). It is noted that all the above magnetic drug-LDH/MFe_2O_4 nanohybrids/nanocomposites either show compact LDH shell morphology without distinguishable LDH nanoplates or display a loosely packed LDH shell with small LDH nanoplates horizontal to the surface of magnetic cores.

Recently, honeycomb-like magnetic hierarchical core@shell structure materials Fe_3O_4@MAl-LDH (M = Mg, CuMg, CuNi) were carefully assembled by our group via a facile low temperature constant pH coprecipitation step (also called the double-drop method) upon the controlled electrostatic interaction.[26−28] The low metal ions concentration and proper solvent effect seemingly play a key role in the oriented LDHs shell nanocrystals over the magnetite cores.[27,28] Shao et al.[29] also reported the hierarchical core@shell LDH microspheres through an extra modification by both SiO_2 and AlOOH to Fe_3O_4 and *in situ* growth of "flower-like" LDH despite it being complex and time-consuming. However, we note in preliminary tests that such stable honeycomb-like core@shell structures are difficult to obtain directly for inorganic-ZnAl-LDH and also are not easy when the drug molecules are taken as the intercalated guests, far from the study on the effect of the shell drug-LDH morphology on the release property, though the uniquely oriented core@shell magnetic organo-LDH hybrids may show an attractive property for wide applications.

Herein, we report the fabrication of nearly monodispersed magnetic hierarchical core@shell salicylate (SA) intercalated ZnAl-LDHs nanovehicles via a modified double-drop coprecipitation method involving hydrolysis of aspirin to SA and the controlled nucleation and oriented growth of SA-LDH nanocrystals over the surface of the larger Fe_3O_4 core (480 nm) upon varied mass ratio (r) of Zn-salt to Fe_3O_4 in a low supersaturation system. The fabricated magnetic nanovehicles Fe_3O_4@SA-LDH-r were thoroughly characterized by combinational techniques. The relationship between the unique morphology and *in vitro* release property with/without external magnetic field is studied and associated with the formation and release mechanisms of the nanovehicles.

2. EXPERIMENTAL SECTION

Materials. Aspirin ($C_9H_8O_4$, Asp, pKa = 3.49) was purchased from Sigma-Aldrich Limited Corporation (Beijing, China); $Zn(NO_3)_2\cdot 6H_2O$, $Al(NO_3)_3\cdot 9H_2O$, and NaAc·$3H_2O$ were from Xilong Chemical Limited Corporation (Guangzhou, China). $FeCl_3\cdot 6H_2O$ was from Tianjin Shentai Chemical Industry Limited Corporation (China), and ethylene glycol and ethanol were from Beijing Chemical Works (China). All reagents were analytical grade and used as available. Decarbonated deionized water was employed by boiling and bubbling N_2 in all synthesis steps.

Synthesis of Magnetic Nanovehicles. The magnetic core Fe_3O_4 sample was preprepared via a surfactant-free solvothermal method previously reported[30] and shows a small BET surface area of 2.2 $m^2\cdot g^{-1}$. The surface site density of the Fe_3O_4 sample was determined from acid−base titrations (details in the Supporting Information). Magnetic nanovehicles were fabricated by the one-step coprecipitation method. A uniform magnetite suspension was obtained by ultrasonically dispersing Fe_3O_4 (0.348 g) nanoparticles in 100 mL of methanol for 15 min and then quickly transferred into a 500 mL four-necked flask. An alkaline solution with NaOH (2.4 g) in 80 mL of methanol was added dropwise into the Fe_3O_4 suspension under vigorous stirring in N_2 flow to modulate the pH to 8.50 and kept for 5 min for stabilization. Then, a mixed salts solution containing $Zn(NO_3)_2\cdot 6H_2O$ (1.34 g), $Al(NO_3)_3\cdot 9H_2O$ (0.56 g), and Asp (0.68 g) in 60 mL of methanol ([Asp]/[Zn^{2+}]/[Al^{3+}] molar ratio of 2.5/3/1) and the above alkaline solution were simultaneously added dropwise into the above Fe_3O_4 suspension under vigorous stirring in N_2 flow keeping constant pH at ~8.5 for 1.5 h. In this situation, Asp can be rapidly hydrolyzed to salicylic acid ($C_7H_6O_3$, pKa_1 = 2.97, pKa_2 = 13.4)[31,32] (Scheme 1).

Scheme 1. Hydrolyzation of Aspirin under Alkaline Condition

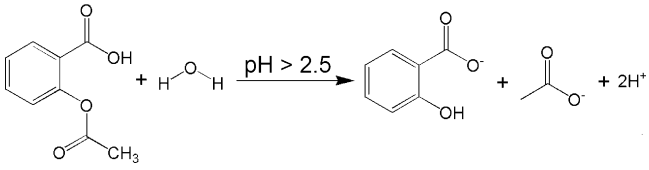

The resultant was aged at 60 °C for 24 h, separated by a magnet of 0.15 T, washed with deionized water until pH ~7.0, and dried in vacuum at 60 °C for 24 h. The products were denoted as Fe_3O_4@SA-LDH-r (r = 1.93, 3.85, and 7.71, refers to the initial mass ratio of Zn-salt to Fe_3O_4). In comparison to Fe_3O_4@SA-LDH-r, the SA intercalated ZnAl-LDH (SA-LDH) was prepared by a similar coprecipitation step without Fe_3O_4.

Characterization. X-ray diffraction (XRD) patterns were recorded on a Rigaku DMAX 2500 diffractometer using Cu Kα radiation (λ = 0.1542 nm, 40 kV, 200 mA) in 2θ 3−70° with a scan speed of 10°/min. Fourier transform infrared spectra (FT-IR) were obtained on a Bruker Vertor 22 spectrophotometer in the range of 4000−400 cm^{-1} with 2 cm^{-1} resolution and 60 scans by the standard KBr disk technique (sample/KBr = 1/100) with almost identical mass of the samples of ~2 mg. The Fourier transform Raman (FT-Raman) spectra were obtained on a Bruker Vertex 70v spectrophotometer at 1064 nm as excitation line in the range of 300−3500 cm^{-1}. The actual metal incorporation contents of the products were measured by inductively coupled plasma (ICP) emission spectroscopy on a Shimadzu ICPS-7500 instrument. CHN microanalysis was carried out using an Elementarvario elemental analysis instrument. The specific surface area was determined by the Brunauer−Emmett−Teller method from a low temperature N_2 adsorption isotherm at 77 K on a Quantachrome Autosorb-1C-VP system. Thermgravimetric analysis (TG) was taken on a PCT-1A instrument with temperature increasing linearly by the

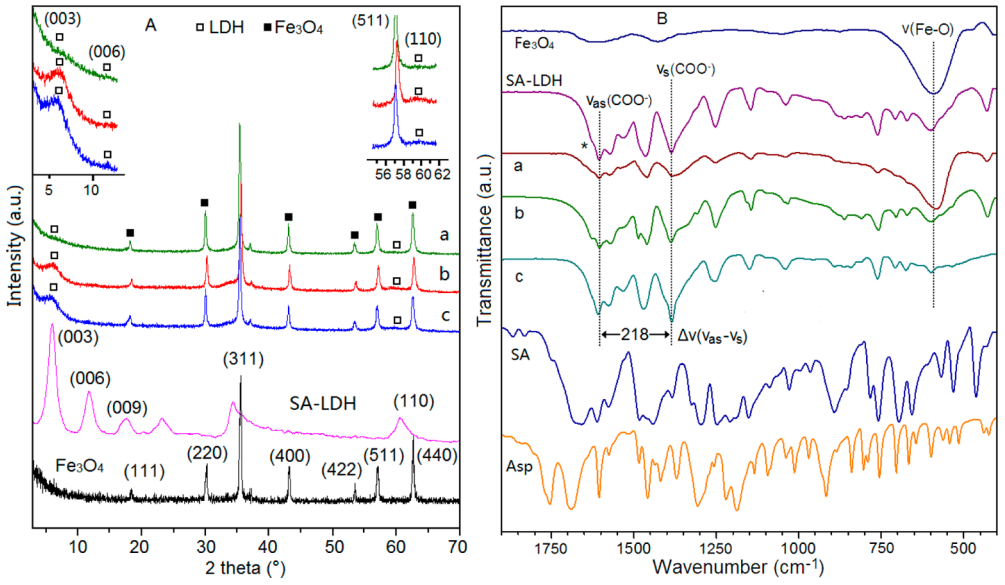

Figure 1. XRD (A) and FT-IR (B, 1900−400 cm^{-1}) spectra of Fe_3O_4@SA-LDH-*r* (a−c: 1.93, 3.85, and 7.71), Fe_3O_4, SA-LDH, SA, and Asp.

rate of 10 °C·min^{-1} from 30 to 700 °C under an air atmosphere. X-ray photoelectron spectra (XPS) were recorded on a Thermo VG ESCALAB250 X-ray photoelectron spectrometer at a base pressure of 2 × 10^{-9} Pa using Al Kα X-ray (1486.6 eV) as the excitation source. All XPS spectra were corrected using the C 1s line at 284.9 eV. SEM-EDX results were obtained on an Oxford Instruments INCAx-act EDX detector attached to a Zeiss Supra 55 field emission scanning electron microscope using a 15 kV electron beam and 60 s acquisition time. Transmission electron microscope (TEM) and HRTEM images were obtained with Hitachi H-800 and JEM-2010, respectively, operated at an accelerating voltage of 120 kV. Magnetic properties of the samples were studied on a Lake Shore 7410 Vibrating Sample Magnetometer at 298 K and 20 kOe applied magnetic field. The determination of the intercalated SA in the nanovehicle was measured by dissolving 0.05 g of the nanovehicle in 250 mL of hydrochloric acid solution (0.2 M) and then analyzed using a Shimadzu UV-2501PC spectrophotometer at 296 nm.

***In vitro* Release Studies.** A solution simulated gastrointestinal and intestinal fluid at pH 7.45/4.60 without pancreatine (phosphate buffered solution (PBS), Chinese pharmacopoeia 2010) was employed as the release medium. The as-fabricated sample (50 mg) was suspended in 250 mL of release medium in a flask and incubated in a water bath at 37 ± 1 °C with paddle rotation speed of 50 rpm. A sample of 3 mL, which was replaced by the same volume of fresh PBS, was withdrawn at specified time intervals and filtered by a hydrophilic filtration membrane to obtain a clear solution for determining the concentration of SA using a standard curve of known concentration of SA.

In order to study the release behavior of the magnetic nanovehicles under the magnetic drug targeting operation, a stable magnetic field (MF: 0.15 T) was applied to emulate the magnetic location and magnetically controlled release process (i.e., "MF on" mode). The magnet was placed just beside the flask, and the position of the magnet relative to the flask was unchangeable during the whole release process. For comparison, the release behavior of single SA-LDH was also estimated.

To understand the release mechanism of SA from the nanovehicles, six release kinetic models were used to fit the *in vitro* release profiles.[9,33,34] (1) The zero-order model, $C_t - C_0 = -k_0 \times t$, usually describes the dissolution process. (2) The first-order model, $\ln(C_t/C_0) = -k_1 \times t$, describes the release from systems where the dissolution rate depends on the drug content in nanohybrids. (3) The parabolic diffusion model, $(1 - C_t/C_0)/t = k_P \times t^{-0.5} + b$, is used to describe diffusion-controlled phenomena in soils and clays with the following equation. (4) The Elovich model, $1 - C_t/C_0 = a\ln t + b$, is applied to chemisorption kinetics of ion-exchange adsorption on soils and clays. (5) The modified Freundlich model, $\log(1 - C_t/C_0) = \log k_F + n\log t$, explains experimental data on ion-exchange and diffusion-controlled process with clays. (6) The Bhaskar model, $\log(C_t/C_0) = -k_B \times t^{0.65}$, can be applied extensively to the release process where the diffusion through the particle is the rate-limiting step. In these models, C_0 and C_t represent the amount of SA in magnetic nanovehicles at a release time of 0 and t, respectively, k is the release rate constant, and a and b are constants, but their chemical significance is not clearly resolved.[21,33,34]

3. RESULTS AND DISCUSSION

Crystal Structure and Chemical Composition. Figure 1A shows the XRD patterns of Fe_3O_4, SA-LDH, and Fe_3O_4@SA-LDH-*r* samples. The XRD of Fe_3O_4 clearly shows sharp lines at 2θ 30.5°, 35.6°, 43.2°, 57.2°, and 62.7° to (220), (311), (400), (511), and (440) planes, respectively, indexed to a typical *fcc* Fe_3O_4 phase (JCPDS 01-1111). The crystal size D_{311} upon Scherrer formula $D_{hkl} = 0.89\lambda/\beta\cos\theta$ (λ is the X-ray wavelength, β is the full-width half-maximum, and θ is the Bragg angle) is 26.8 nm, close to the critical size of ~30 nm of single magnetite domains,[35] implying the superparamagnetic property of the Fe_3O_4 particles. The XRD of SA-LDH shows sharp lines at 2θ 6.0°, 11.8°, 17.6°, and 60.8° to (003), (006), (009), and (110) planes, respectively, clearly showing the formation of the *hcp* LDH phase.[1,36] The small peak at ~23.7° is probably due to the presence of a small amount of CO_3-LDH which often occurs even under N_2 protection.[1,9] The much larger basal spacing, d_{003}, of SA-LDH (1.47 nm) compared to CO_3-LDH (0.75 nm)[20] clearly indicates the successful intercalation of SA anions into LDH interlayers, though this value is slightly smaller than that previously reported for salicylate-Mg_2Al-LDH (1.63 nm)[36] probably due to the lower layer charge density x (Table S1 in the Supporting Information) in the present SA-LDH (Zn/Al = 3). For the magnetic nanovehicles Fe_3O_4@SA-LDH-*r* (r = 1.93, 3.85, 7.71) (Figure 1A(a−c)), besides the sharp lines of the Fe_3O_4 phase, weak (003) line at ~6.1° and (110) line at ~60.0° of the SA-intercalated LDH phase can be carefully distinguished in the enlarged pattern with close d_{003} values of 1.36, 1.38, and 1.40 nm, corresponding to their approximate layer charge density x

dx.doi.org/10.1021/am506113s | ACS Appl. Mater. Interfaces 2014, 6, 20498−20509

(Table S1 in the Supporting Information). These d_{003} values are all smaller than that of pure SA-LDH probably owing to the interaction between the LDH and Fe_3O_4 phase. A similar phenomenon has been observed in 5-ASA-LDH/$MgFe_2O_4$.[20] The weak (003) line makes it difficult to obtain the Scherrer dimension (D_{003}) of LDH phase in Fe_3O_4@SA-LDH-1.93 while the D_{003} values of Fe_3O_4@SA-LDH-3.85 and Fe_3O_4@SA-LDH-7.71 are 5.96 and 6.56 nm, respectively, similar to that of pure SA-LDH (D_{003} = 5.83 nm). However, the I_{110}/I_{003} values (intensity ratio of (110) to (003) line) for Fe_3O_4@SA-LDH-*r* samples within 0.33−0.76 are obviously larger than pure SA-LDH (0.25) and lower than previous Fe_3O_4@MgAl-LDH (1.25),[26] implying the possible oriented growth of the SA-LDH nanocrystals over the surface of Fe_3O_4.

Figure 1B shows the FT-IR spectra of Fe_3O_4@SA-LDH-*r* and related samples in 1900−400 cm^{-1}. The FT-IR of Fe_3O_4 clearly shows a strong band at 590 cm^{-1} due to the Fe−O lattice mode. The FT-IR of SA-LDH reveals a strong broad band around 3440 cm^{-1} (unshown) assigned to the stretching mode of the structural −OH group of LDH layers and interlayer H_2O, and the band at 429 cm^{-1} to the M−OH lattice mode of the LDH layers. The strong bands at 1604 cm^{-1} (a shoulder (*) at 1630 cm^{-1} assigned to δ_{H2O}) and 1385 cm^{-1} can be ascribed to antisymmetric stretching (ν_{as}) and a symmetric one (ν_s) of the $-COO^-$ groups.[20,37,38] Compared to $\nu_s(COO^-)$ of sodium salicylate (1403 cm^{-1}),[39] the redshift in SA-LDH can be ascribed to the hydrogen bond between $-COO^-$ groups of SA^- ions and −OH groups of the LDH layers.[37] However, neither the IR band of ν(COOR) (1755 cm^{-1}) nor the FT-Raman bands (Figure S1 in the Supporting Information) of ν(COOR) (1760 cm^{-1}) and $\nu(CH_3)$ (2942 and 2991 cm^{-1}) of pure Asp are observed, clearly confirming the complete hydrolysis of raw Asp to SA.[40,41] The $\Delta\nu$ ($\nu_{as} - \nu_s$) of the $-COO^-$ group in SA-LDH is 218 cm^{-1}, close to that of sodium salicylate (193 cm^{-1}),[39] indicating that the SA^- ions bridge to the layer hydroxyls with both oxygen ions of carboxylate.[37] The bands at 1574 and 1459 cm^{-1} can be assigned to ν(C=C) of the benzene ring, and the bands at 1253 and 1037 cm^{-1} are assigned to ν(C−O) while that at 1145 cm^{-1} is assigned to ν(C−H) associated with the p−π conjugation of phenolic hydroxyls. The bands at 890, 758 (*o*-substituted), 697, 570, and 463 cm^{-1} can be assigned to the in-plane and out-plane δ(C=C) of the benzene ring.[40]

Then, as predicted, the magnetic nanovehicles Fe_3O_4@SA-LDH-3.85 and Fe_3O_4@SA-LDH-7.71 (Figure 1B(b,c)) exhibit quite similar IR bands to those of SA-LDH, while Fe_3O_4@SA-LDH-1.93 (Figure 1B(a)) shows weak absorptions of SA-LDH and strong ν(Fe−O) from Fe_3O_4, implying varied contents of SA-LDH and Fe_3O_4 phases in the Fe_3O_4@SA-LDH-*r* samples. Interestingly, Fe_3O_4@SA-LDH-3.85 shows nearly identical $\nu_{as}(COO^-)$ and $\nu_s(COO^-)$ positions to SA-LDH, while the others show slightly red-shifted $\nu_{as}(COO^-)$, implying slightly varied host (LDH)−guest (SA) interaction existing in Fe_3O_4@SA-LDH-*r* samples upon the incorporation of Fe_3O_4. Considering the close gallery height (= d_{003} − 0.48 nm) values in 0.89−0.92 nm for Fe_3O_4@SA-LDH-*r* to the dimension of SA (~0.89 nm) (Figure S2 in the Supporting Information), together with the higher surface area per unit charge of the layer (0.334 nm^2/charge) (Table S1 in the Supporting Information) compared to salicylate (0.287 nm^2/charge),[36] a bidentatedly bridged mode with vertical monolayer of SA anions linked to the layers is tentatively proposed upon the electrostatic interactions between the carboxyl groups and the brucite-like layers along with the hydrogen bond and van der Waals force.

Upon the CHN analysis, the Fe_3O_4@SA-LDH-*r* (*r* = 1.93, 3.85, and 7.71) possess drug loadings of 2.7, 3.3, and 5.5 wt %, respectively (Table S1 in the Supporting Information), near to those from UV analysis on acid dissolved samples. Though much lower than pure SA-LDH (19.2 wt %) owing to the massive magnetite portion of 19.2−34.5 wt % (ICP) and also lower than chitosan-SA nanoparticles (20−25 wt %),[42] these SA loadings are quite close to previously reported L-phenylalanine-derived supramolecular SA hydrogels (10%)[43] and SA-bentonite and SA-kaolin complexes (5−8%);[44] thus, the Fe_3O_4@SA-LDH-*r* nanovehicles can be used as potential magnetically targeted drug delivery vehicles despite relatively large amounts of materials needed for delivering a useful therapeutic dose. Considering the small discrepancy in the layer charge density of magnetic nanovehicles (Table S1 in the Supporting Information), the obviously varied SA loadings can be ascribed to the varied portions of LDH phase upon initial *r* (=$W_{Zn\text{-}salt}/W_{Fe3O4}$) values and may also relate to their LDH nanoplates stacking modes.

Morphology and Core−Shell Interactions. The SEM and TEM images of Fe_3O_4@SA-LDH-*r* samples are shown in Figure 2. The nearly monodispersed Fe_3O_4 particles (Figure S3 in the Supporting Information) have a smooth spherical surface and much larger diameter of 480 nm than the previously reported magnetic core in magnetic LDH nanohybrids.[20,22−25] While the pure SA-LDH (Figure S4 in the Supporting Information) shows severely aggregated plate-like particles with the size of 100−200 nm, all the Fe_3O_4@SA-LDH-*r* samples exhibit a well-defined core@shell structure with light

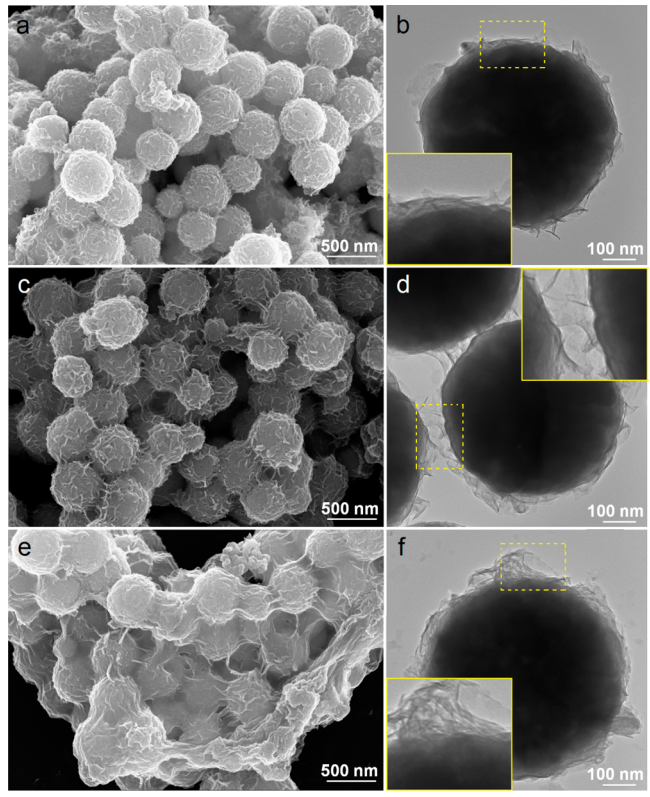

Figure 2. SEM (a, c, e) and TEM (b, d, f) images of Fe_3O_4@SA-LDH-*r* (a, b: 1.93; c, d: 3.85; e, f: 7.71).

dx.doi.org/10.1021/am506113s | ACS Appl. Mater. Interfaces 2014, 6, 20498−20509

gray LDH nanocrystals tightly attached to dark Fe_3O_4 cores in varied growth orientations affording to a rough surface. Apparently, the incorporation of the Fe_3O_4 core particles make the LDH shell nanocrystals better dispersed compared to pure SA-LDH. For Fe_3O_4@SA-LDH-1.93 (Figure 2a,b), it can be clearly seen that the hexagonal SA-LDH nanocrystals stack closely with the *ab*-face mainly horizontal to the surface of Fe_3O_4 forming a compact thin shell of ca. 20 nm with LDH plate thickness of ∼5.2 nm and size of ∼32 nm. Then, for Fe_3O_4@SA-LDH-3.85 (Figure 2c,d), very thin SA-LDH nanocrystals stack regularly with the *ab*-face mainly vertical to the surface of Fe_3O_4 forming a thicker "floss-like" shell of ca. 45 nm with an LDH plate thickness of ∼4.1 nm (close to the D_{003} of 5.96 nm) and size of ∼46 nm. EDX mapping analysis (Figure S5 in the Supporting Information) clearly shows that iron is located in the center with a spherical outline of Fe_3O_4 cores, while Zn and Al are uniformly distributed in the whole particles. Then, for Fe_3O_4@SA-LDH-7.71 (Figure 2e,f), the SA-LDH nanocrystals stack randomly with the *ab*-face vertical/slant/horizontal to the surface of Fe_3O_4 forming a cross-linking thick shell of ca. 40−60 nm with LDH plate thickness of ∼3.3−6.2 nm (close to the D_{003} of 6.56 nm) and size of ∼35−64 nm probably due to its highest concentrations of both Zn^{2+} ions and the organic guest in the synthesis system.

The HRTEM images further reveal the detailed core@shell interface feature of the magnetic nanovehicles. Typically, Fe_3O_4@SA-LDH-3.85 (Figure 3a) shows a gray shell consisting

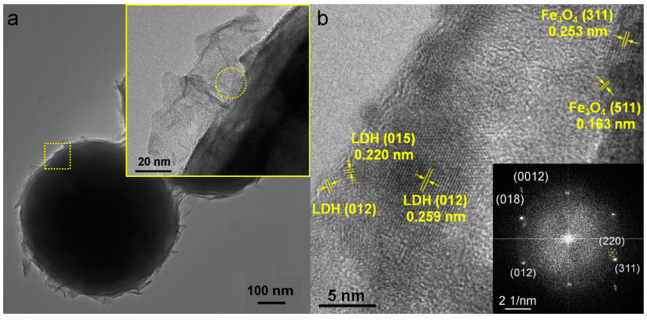

Figure 3. (HR)TEM images of Fe_3O_4@SA-LDH-3.85 with varied magnification (a, b).

of a monolayer thin SA-LDH nanoplate vertically interdigitated toward the core surfaces. Figure 3b shows the lattice fringes for the core−shell interface region. As expected, the clearly consecutive lattice fringes observed with the spacing of 0.163 and 0.253 nm are indexed to the (511) and (311) planes of the *fcc* Fe_3O_4 phase (JCPDS No. 01-1111) and 0.220 and 0.259 nm are indexed to the (015) and (012) planes of the hexagonal LDHs phase (JCPDS No. 38-0486), in line with the SAED result (Figure 3b, inset), indicating that the hexagonal LDH nanocrystals hold good crystallinity after assembling onto the surface of Fe_3O_4 with special growth orientations. This is the first report on organo-LDH with varied LDH nanoplate orientations on the Fe_3O_4 surface; specially, the latter two samples are quite different from the previously reported core−shell magnetic drug-LDH/$MgFe_2O_4$ nanohybrids[20,22,23,25] but somewhat similar to the honeycomb-like Fe_3O_4@CO_3-LDH magnetic supports.[26−28] The varied morphologies of the Fe_3O_4@SA-LDH-*r* magnetic nanovehicles may account for the slightly varied host−guest and core−shell interactions.

In order to figure out the core−shell interaction, the Zn 2p, Al 2p, Fe 2p, and C 1s XPS spectra of Fe_3O_4@SA-LDH-*r* and related samples were obtained (Figure 4 and Table S2 in the Supporting Information). For pure SA-LDH, Zn $2p_{3/2}$ and Al $2p_{3/2}$ locate at the binding energy (BE) of 1021.9 and 74.4 eV, respectively, indicating the presence of Zn^{2+} and Al^{3+} ions,[20] while the Fe $2p_{3/2}$ at 710.4 eV is typical for Fe_3O_4.[30] Then, for Fe_3O_4@SA-LDH-1.93, the Zn $2p_{3/2}$ at 1022.2 eV and Al $2p_{3/2}$ at 74.7 eV, both 0.3 eV higher than those of pure SA-LDH, are assigned as the "Zn−O−Al" linkage, while the BE value of Fe $2p_{3/2}$ is 709.9 eV, 0.5 eV lower than Fe_3O_4. These BE changes reveal relatively lower electron density around Zn and Al atoms and the higher electron density around Fe atoms, illustrating a possible interaction between the LDH shell and magnetite core. According to the elemental electronegativity order of Fe (1.83) > Zn (1.65) > Al (1.61), it can be conjectured that there might be a "Zn(Al)−O-Fe" linkage between the Fe_3O_4 core and the SA-LDH shell similar to that previously reported for 5-ASA-LDH/$MgFe_2O_4$.[20] The weak peak at 1025.8 eV can be assigned to the "Zn−O−C" linkage.[45] While for Fe_3O_4@SA-LDH-3.85, the sharp and symmetrical peak of Zn $2p_{3/2}$ at 1022.0 eV, quite close to that of SA-LDH, indicates all Zn atoms existed in the LDH phase, together with the Fe $2p_{3/2}$ BE value, very close to that of Fe_3O_4, suggesting a much weaker electron-transfer effect in this sample probably due to the thicker LDH shell leading to the weak core−shell interaction compared to Fe_3O_4@SA-LDH-1.93. As for Fe_3O_4@SA-LDH-7.71, the BE value of Zn $2p_{3/2}$ is 0.4 eV higher than SA-LDH, while the Fe $2p_{3/2}$ cannot be detected owing to its much thicker cross-linking LDH shell as the TEM shows. While the evident peak at 1021.4 eV can be assigned to amorphous ZnO,[45] it implies a complex shell composition including SA-LDH and amorphous ZnO for the sample Fe_3O_4@SA-LDH-7.71.

As discussed above, Fe_3O_4@SA-LDH-1.93 with the LDHs nanocrystals closely stacked with the *ab*-face horizontal to the surface of Fe_3O_4 can be rationally ascribed to the strong core−shell interaction via the "Zn(Al)-O-Fe" linkages. Comparatively, Fe_3O_4@SA-LDH-3.85 with the LDHs nanocrystals loosely stacked with the *ab*-face mainly vertical to the core surface is related to the weaker core−shell interaction considering the existence of the "Zn(Al)-O-Fe" linkages specially at the internal core−shell interface. While Fe_3O_4@SA-LDH-7.71 with the LDH shell particles vertical/slant/horizontal to the core surfaces, along with partial amorphous ZnO phases, afford its complex and strong core−shell interactions. The C 1s XPS fittings clearly reveal the presence of O−C═O, C−OH, and C−C/C-H bonds belonging to the carboxyl, hydroxyl, and benzene ring, respectively, of pure SA.[46] Moreover, compared to SA-LDH, nearly unchanged C 1s BE (289.0 eV) due to $-COO^-$ groups in Fe_3O_4@SA-LDH-3.85 implies similar host−guest interactions to SA-LDH in line with their close layer charge density (Table S1 in the Supporting Information) despite the hybridization of Fe_3O_4, while the reduced C 1s BE values in Fe_3O_4@SA-LDH-1.93 (288.5 eV) and Fe_3O_4@SA-LDH-7.71 (287.3 eV) reveal the slightly stronger host−guest interaction though the latter apparently holds high Zn/Al ratio (lower *x*) that may be overestimated due to the presence of partial ZnO species. These results are intimately related to the varied morphologies of the present magnetic nanovehicles upon the unique synthesis strategy and formation mechanism.

Formation Mechanism. This is the first report on organo-ZnAl-LDH-based hierarchical core@shell structural magnetic nanohybrids with controlled LDH shell growth orientations.

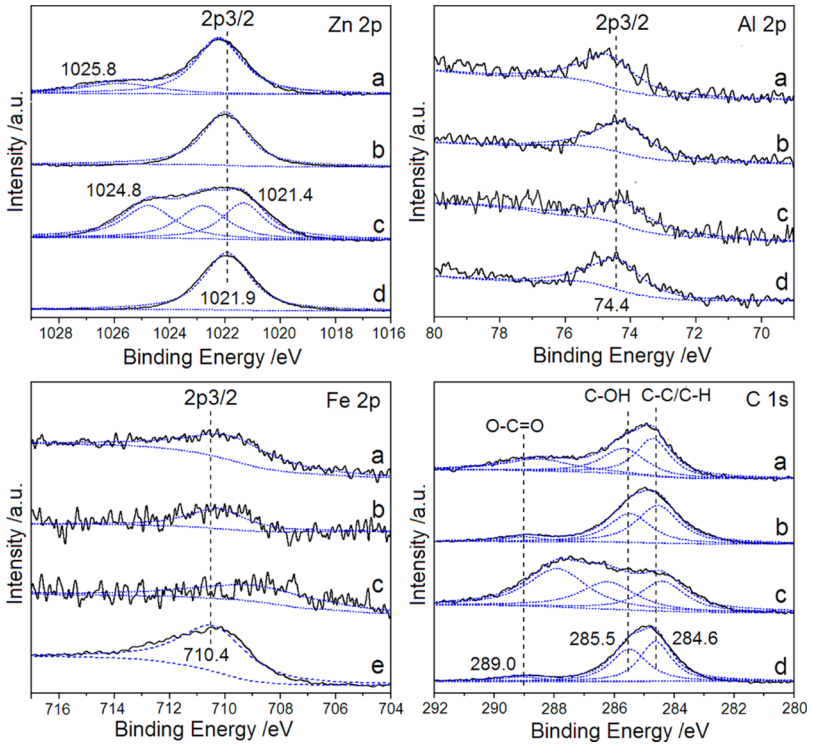

Figure 4. Zn $2p_{3/2}$, Al $2p_{3/2}$, Fe $2p_{3/2}$, and C 1s XPS spectra of Fe_3O_4@SA-LDH-*r* (a–c: 1.93, 3.85, 7.71), SA-LDH (d), and Fe_3O_4 (e).

Apparently, the nearly monodispersed Fe_3O_4 core particles (480 nm) (Figure S3 in the Supporting Information) may provide more accessible solid/liquid interface than those easily aggregated small magnetic nanoparticles in previous magnetic drug-LDH nanohybrids[20−23] for uniformly heterogeneous nucleation upon modified adsorption of metal ions.[47] In detail, the Fe_3O_4@SA-LDH-*r* nanovehicles were fabricated by a modified double-drop coprecipitation method through four main steps: (i) the negatively charged modification of Fe_3O_4 surfaces by tuning pH to ∼8.5 of Fe_3O_4-methanol suspension (pI 6.5 of Fe_3O_4 suspension[26]); (ii) adsorption of Zn^{2+} or Al^{3+} ions onto the core surfaces via the electrostatic attraction; (iii) simultaneous hydrolysis of raw Asp to SA in alkaline solution and the nucleation of SA-LDH nanocrystals onto the core surfaces; (iv) aging and Ostwald ripening of SA-LDH nanocrystals on the surface of Fe_3O_4.

As shown in Table S3 (in the Supporting Information), the ion products $[Zn^{2+}][OH^-]^2$ (3.75×10^{-16} to 1.5×10^{-15}) and $[Al^{3+}][OH^-]^3$ (3.95×10^{-23} to 1.19×10^{-22}) in the double-drop coprecipitation system of Fe_3O_4@SA-LDH-*r* are higher than the solubility product (K_{sp}) of $Zn(OH)_2$ (3.0×10^{-17}) and $Al(OH)_3$ (1.33×10^{-33}), respectively, implying the easy coprecipitation of both metal ions. However, these values are much lower than those in the synthesis of most Zn-based LDH such as lactate-ZnAl-LDH,[48] IBU-ZnAl-LDH,[9] CO_3-ZnAl-LDH,[49] 5-ASA-ZnAl-LDH,[38] and 5-ASA-ZnAl-LDH/$MgFe_2O_4$ nanohybrid,[20] clearly indicating the much lower supersaturation kept throughout the present double-drop coprecipitation process. Similar phenomena can also be found in the magnetic MgAl-LDH system, such as hierarchical structural Fe_3O_4@CO_3-MgAl-LDH,[26] with a much lower ion product $[Mg^{2+}][OH^-]^2$ of 4.5×10^{-13} (close to the K_{sp} of $Mg(OH)_2$ (5.6×10^{-12})) than those of IBU-MgAl-LDH/$MgFe_2O_4$ and DIC-MgAl-LDH/$MgFe_2O_4$ nanohybrids.[22,23] Also, the much lower K_{sp} of $Zn(OH)_2$ than $Mg(OH)_2$ implies that it is much easier for Zn-based hydroxide to reach the precipitation conditions. Actually, at the present low Zn^{2+} ions level (i.e., $[Zn^{2+}][OH^-]^2 = 7.5 \times 10^{-16}$ for Fe_3O_4@SA-LDH-3.85), the homogeneous nucleation rate (J) of $Zn(OH)_2$ reaches 2.914×10^9 (Table S4 in the Supporting Information), while Mg^{2+} ions cannot be precipitated upon the classical nucleation theory.[50] Even at an elevated ions level, the nucleation rate of $Zn(OH)_2$ is much higher than that of $Mg(OH)_2$ (J' in Table S4 in the Supporting Information). It can be deduced that ZnAl-LDH may have a much faster nucleation rate than MgAl-LDH even in a heterogeneous system using Fe_3O_4 as core particles, thus leading to greatly increased difficulty to directly coprecipitate ZnAl-LDH nanocrystals onto the surfaces of magnetite cores compared to the MgAl-LDH system as our preliminary tests experienced.

Therefore, in this work, we carefully design a low supersaturation system to tune the nucleation rate of Zn-based LDH and control the particle size and growing orientation of ZnAl-LDH onto the surfaces of Fe_3O_4, effectively assembling a series of relatively stable and LDH oriented grown hierarchical core@shell structured Fe_3O_4@SA-LDH-*r* nanovehicles. Meanwhile, the use of methanol is also a benefit for the formation of the Fe_3O_4@SA-LDH hierarchical structure by reducing the crystal growth rate, as previously reported that the polar solvent molecules (ethanol, ethylene, glycol, etc.) can be strongly adsorbed on the primarily formed LDH particle surfaces and inhibit the accessibility to metal ions thus suppressing the crystal growth.[51] Thus, this is a novel organic solvent-assisted interface-controlled organo-LDH assembly process on the core surfaces, and it is possible to obtain a morphology-controlled Zn-based LDH core@shell structure by tuning the metal ions level on a solid–liquid interface via modulating the mass ratio (r) of metal salt to magnetite.

On the basis of acid–base titrations (Figure S6 and S7, details in the Supporting Information),[52] the determined

surface OH site density (D_s) of the present Fe_3O_4 core particles is 17 site·nm^{-2}, which is close to the 15−19 OH site·nm^{-2} for γ-Al_2O_3,[53] though higher than the 4−10 OH site·nm^{-2} for common hydroxyl oxides surfaces including α-Fe_2O_3 and SiO_2 etc.[54] Combinational consideration of the charge, ionic radius, and electronegativity of the Zn^{2+} ion (0.074 nm, 1.65) and Al^{3+} (0.050 nm, 1.61), along with the Zn/Al ratio of 3 in the present supersaturation system, Zn^{2+} and Al^{3+} ions tend to be simultaneously adsorbed on the surface of the Fe_3O_4 core via electrostatic attraction.[47,55] Assuming a 100% adsorption of Zn^{2+} and Al^{3+} ions from each drop of the mixed salts solution onto the surface of the Fe_3O_4 core in the present low supersaturation system, the surface OH sites occupied by Zn^{2+} and Al^{3+} ions via electrostatic attraction can be estimated as 8.8, 17.7, and 35.4 site·nm^{-2}, respectively, for Fe_3O_4@SA-LDH-*r* nanovehicles with varied *r* values from 1.93 to 3.85 and 7.71. Clearly, the surface OH sites occupied by Zn^{2+} and Al^{3+} ions on the Fe_3O_4 surface during the synthesis of Fe_3O_4@SA-LDH-1.93 is much lower than the D_s of the Fe_3O_4 core (17 site·nm^{-2}) thus leading to a thin compactly stacked LDH shell with the *ab*-face horizontal to the Fe_3O_4 surface probably owing to the smaller spacial resistance and weak ion−ion repulsion. Although that for Fe_3O_4@SA-LDH-3.85 is very close to the D_s of Fe_3O_4 thus resulting in a loosely stacked LDH shell with the *ab*-face mainly vertical to the Fe_3O_4 surface, that for Fe_3O_4@SA-LDH-7.71 is higher than the D_s of Fe_3O_4 therefore causing a severely cross-linked LDH shell with the *ab*-face vertical/slant/parallel to the Fe_3O_4 surface owing to the larger spacial resistance. Clearly, with increasing *r* values, LDH shell nanocrystals become thinner and larger affording to the mainly vertical cross-linked LDH shell morphology.

Figure 5 schematically presents a formation mechanism of the SA-ZnAl-LDH oriented grown hierarchical core@shell structured Fe_3O_4@SA-LDH-*r* magnetic nanovehicles. Under low supersaturation condition, such as the present double-drop coprecipitation systems with $[Zn^{2+}][OH^-]^2$ in 3.75 × 10^{-16} to 1.5 × 10^{-15} corresponding to *r* values in 1.93−7.71, the relative amount of metal salt to Fe_3O_4 plays a key role in the electrostatic attraction of metal ions and the followed Ostwald ripening of organo-LDHs, which mainly results in varied organo-LDH shell morphologies. Similar LDH oriented hierarchical core@shell structures with L-lactic acid intercalated ZnAl-LDH and SA intercalated Mg_3Al-LDH assembling on the surface of Fe_3O_4 are also successfully fabricated by using the present strategy (Figure S8 in the Supporting Information).

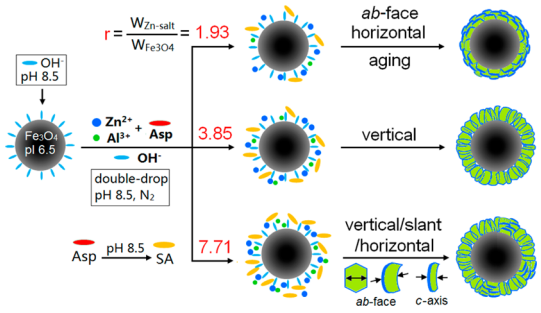

Figure 5. Formation mechanism of Fe_3O_4@SA-LDH-*r* magnetic nanovehicles.

Thermal Stability. Figure 6 shows the TG/DTA curves of Fe_3O_4@SA-LDH-*r* samples in ambient atmospheres. Figure S9 (in the Supporting Information) gives the TG/DTA curves of pure SA and SA-LDH. For solid salicylic acid (Figure S9A in the Supporting Information), the whole weight loss process exhibits an endothermic event. An intense endothermic peak at ~186 °C closely connected with another one at 213 °C can be ascribed to the melting and boiling of the SA, similar to a previously reported melting point within 158−161 °C.[32] While for SA-LDH (Figure S9B in the Supporting Information), a weak endothermic peak around 106 °C can be ascribed to the removal of a small amount of physisorbed water and major interlayer water, and a next endothermic peak at 275 °C is due to the removal of residual interlayer water and partial dehydroxylation of the LDH layer.[20] A rapid mass loss in 350−550 °C can be assigned to the decomposition and combustion of the interlayer SA guests, corresponding to a strong exothermal peak at 432 °C. Dehydroxylation of the LDH layers usually occurs between 300 and 500 °C,[36] but the corresponding endothermic event is probably canceled by the strong exothermic one due to the drug combustion. Differently, the TG/DTA plots of Fe_3O_4@SA-LDH-*r* (Figure 6) clearly show five stages. A faint mass loss before 200 °C can be assigned to the removal of a small amount of physisorbed water and major interlayer water, and a continuous one in 200−310 °C assigned to the removal of residual interlayer water and partial dehydroxylation of the layer. A rapid mass loss in 310−420 °C corresponding to a strong exothermic event at ~380 °C can be attributed to the SA decomposition and the layer dehydroxylation. Clearly, the SA decomposition/combustion temperatures in SA-LDH (432 °C) and Fe_3O_4@SA-LDH-*r* (~380 °C) are much higher than the melting point of SA, indicating that the host−guest interaction could greatly promote the thermal stability of the interlayer SA guest. Moreover, the decomposition/combustion of SA in Fe_3O_4@SA-LDH-*r* samples is much easier than in SA-LDH, which can

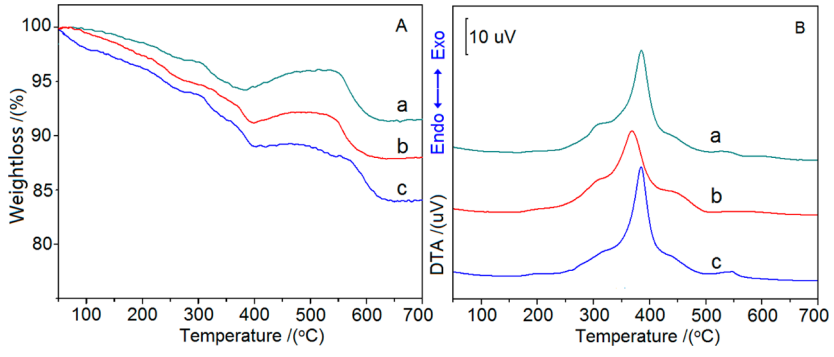

Figure 6. TG (A) and DTA (B) curves of Fe_3O_4@SA-LDH-*r* samples (a−c: 1.93, 3.85, and 7.71).

be ascribed to a better dispersion of SA-LDH nanocrystals on the large magnetite cores, compared to the aggregated pure SA-LDH. The lowest decomposition temperature of SA in Fe_3O_4@SA-LDH-3.85 (368 °C) strongly suggests that the vertically oriented SA-LDH shell nanocrystals in this sample is more favored for heat delivery compared to the other two samples. As for a slow mass increase and the followed mass loss in 400−600 °C corresponding to two weak exothermic peaks at ∼450 and 545 °C, it can be assigned to the phase transformation from Fe_3O_4 to γ-Fe_2O_3[56] and the combustion of residual SA, respectively.

Magnetic Property. Figure 7 displays the room temperature magnetization curves of Fe_3O_4 and Fe_3O_4@SA-LDH-*r*

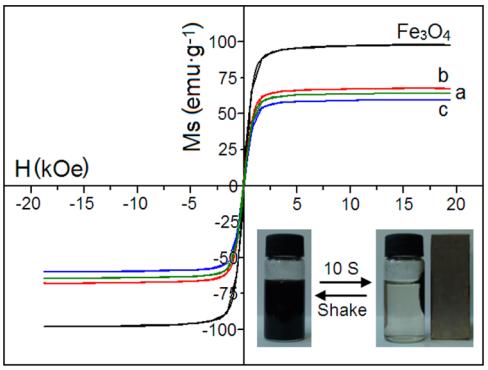

Figure 7. Room temperature magnetization curves of Fe_3O_4@SA-LDH-*r* (a−c: 1.93, 3.85, 7.71) and Fe_3O_4 (photos refer to separation/redispersion of the sample upon a 0.15 T magnet).

nanovehicles. The magnetic saturation (M_s) of the Fe_3O_4 sample is 98.2 emu·g^{-1}, slightly higher than that of bulk magnetite (92 emu·g^{-1}).[30,57] The strong superparamagnetism with weak coercive force and remanence is consistent with the Scherrer dimension D_{311} of Fe_3O_4 core particles (26.8 nm), which is near to the critical single domain size (30 nm).[35] The M_s of Fe_3O_4@SA-LDH-*r* is significantly reduced owing to the shielding effect of the nonmagnetic SA-LDH shell. It is noted that the M_s values of these nanovehicles obey an order of Fe_3O_4@SA-LDH-3.85 (67.7 emu·g^{-1}) > Fe_3O_4@SA-LDH-1.93 (64.3 emu·g^{-1}) > Fe_3O_4@SA-LDH-7.71 (59.7 emu·g^{-1}) though Fe_3O_4@SA-LDH-3.85 possesses a moderate thickness of the SA-LDH shell probably owing to its lowest shell packing density originating from the LDH *ab*-face vertical to the surface of Fe_3O_4 and thus having the smallest magnetic shielding effect. These magnetic nanovehicles can be rapidly separated by an external magnetic field and easily redispersed in water or alcohol by shaking after removing the magnetic field, indicating the good superparamagnetism of the Fe_3O_4@SA-LDH-*r* samples inherited from the Fe_3O_4 core particles and therefore being quite suitable for the drug controlled release.

Controlled Release Property. Figure 8 depicts the release profiles of Fe_3O_4@SA-LDH-*r* magnetic nanovehicles and pure SA-LDH under no external magnetic field ("no MF") and with MF ("MF on") modes at 37 ± 1 °C. All the profiles exhibit a fast release stage at the initial 15 min (inset in Figure 8) followed by a slow stable one until a constant accumulated release percentage (i.e., equilibrium release amount, rel_{eq}) at 7.5 h. Under "no MF" mode, the release profile of SA-LDH shows a stable release process with a rel_{eq} of 56.9% and a $t_{0.5}$ (the time for release fraction of 50%) of 13.5 min. However, Fe_3O_4@SA-LDH-3.85 and Fe_3O_4@SA-LDH-7.71 exhibit slightly decreased

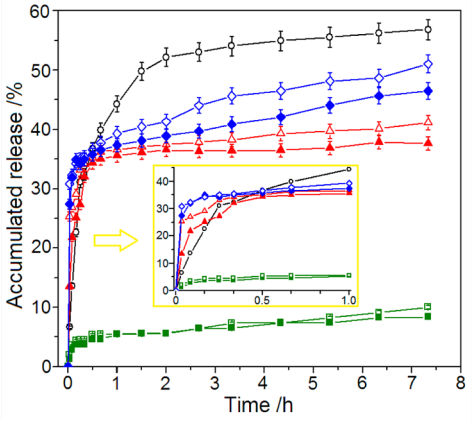

Figure 8. *In vitro* release profiles of SA-LDH (hollow circle) and Fe_3O_4@SA-LDH-*r* (1.93: square; 3.85: triangle; 7.71: diamond) in pH 7.45 PBS (solid: MF on; hollow: no MF).

rel_{eq} of 41.2% and 51.1% but greatly reduced $t_{0.5}$ of 1.63 and 1.66 min compared to SA-LDH, respectively, corresponding to their much faster initial release rates (inset in Figure 8). The much faster initial release rate of these two samples than SA-LDH may be attributed to their well dispersed thin SA-LDH nanocrystals on the surfaces of Fe_3O_4 cores compared with the aggregated pure SA-LDH facilitating the exchange process of the interlayer SA anions with phosphate ions in PBS. Meanwhile, the weaker interparticle interaction of LDH shell nanocrystals in these two samples obviously shortens the release path of SA and reduces the release resistance. While Fe_3O_4@SA-LDH-1.93 shows a dramatically reduced SA release (10.0%) and greatly elongated $t_{0.5}$ (25.6 min), which is probably due to its closely stacked horizontal LDH shell nanocrystals and thus stronger LDH interparticle interaction and slightly stronger host (LDH)−guest (SA) interaction compared with other samples.

It is noted that, for all the samples even pure SA-LDH, the rel_{eq} cannot reach 100% even below 80%. This is because the easily formed grafting of phosphate ions to the ZnAl-LDH layers, clearly proved by a strong IR band at 1050 cm^{-1} owing to the ν_3(P−O) stretching of the recovered sample after the release test (Figure S10 in the Supporting Information), similar to that previously observed in adsorption of CO_3(Cl, NO_3)-ZnAl-LDH toward phosphate,[58,59] leads to an immobilized interlayer moiety thus inhibiting the release of the inner SA guests. However, these rel_{eq} values are still much higher than the previously reported bentonite-SA (1.4% at 23 h in homoionic solution)[44] possibly due to the higher anion exchange capacity of LDH materials, implying the good drug-delivery ability of the present magnetic nanovehicles.

However, under the "MF on" mode, three Fe_3O_4@SA-LDH-*r* samples show different changes in release behavior compared to those under "no MF" mode. All the samples present some decrease in rel_{eq} values (8.4−46.6%) though with nearly the same $t_{0.5}$ as those under "no MF" mode, implying the existence of the MF effect on the release property of Fe_3O_4@SA-LDH-*r* nanovehicles. Differently, only Fe_3O_4@SA-LDH-3.85 shows a clear release decrease from the initial release stage, indicating strong MF retarding effect corresponding to its largest M_s value, while others show this suppressed effect until ca. a 1 h release time. These phenomena are somewhat varied from the previously reported magnetic drug-LDH.[20,22,23] The less pronounced retarding effect of external MF on drug release

from the present magnetic nanovehicles is somewhat due to the obviously reduced particle−particle magnetic interactions owing to the larger magnetic core size (480 nm) and the uniquely oriented LDH shell of Fe_3O_4@SA-LDH-*r* nanovehicles.

We also tested the drug release behaviors of the Fe_3O_4@SA-LDH-*r* and SA-LDH in pH 4.60 PBS (Figure S11 in the Supporting Information). All the samples show greatly enhanced release rate and release percentage. The rel_{eq} of SA-LDH at 7.5 h reaches 73.2%, higher than that at pH 7.45 (56.9%), while the rel_{eq} values of Fe_3O_4@SA-LDH-1.93, Fe_3O_4@SA-LDH-3.85, and Fe_3O_4@SA-LDH-7.71 are 82.7%, 93.3%, and 95.2%, respectively, much higher than those at pH 7.45 (10%, 41.2%, and 51.1%). These phenomena may be attributed to the partial dissolution of LDH layers at weak acidic solutions quite similar to the previously reported release behavior of captopril-MgAl-LDH in pH 4.60 PBS.[11]

Release Mechanism. To understand the release mechanism of these magnetic nanovehicles, in vitro release data at pH 7.45 were fitted to several kinetic models.[22,23,33,34] The zero-order and the first-order models are not suitable to explain the whole release of all the samples reflected by small linear correlation coefficients of $R^2 < 0.80$ under both "no MF" and "MF on" modes, suggesting that the drug release is not a single dissolution or diffusion process. From Figure 9 and Table 1, it can be seen that the Elovich model fits well the release data of all the samples ($R^2 > 0.94$) especially the pure SA-LDH ($R^2 = 0.97$), implying the existence of a bulk and surface diffusion process for all the samples.

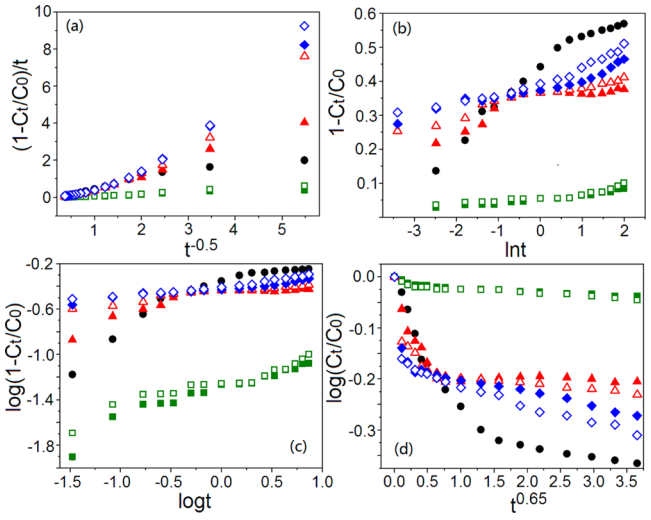

Figure 9. Plots of kinetic models of (a) parabolic diffusion, (b) Elovich, (c) modified Freundlich, and (d) Bhaskar for release data of Fe_3O_4@SA-LDH-*r* (1.93: square; 3.85: triangle; 7.71: diamond) and SA-LDH (dot) in pH 7.45 PBS (solid: MF on; hollow: no MF).

For Fe_3O_4@SA-LDH-1.93 and Fe_3O_4@SA-LDH-3.85, the parabolic and modified Freundlich models also give the better fits, especially the Parabolic diffusion model under both "no MF" and "MF on" modes especially "MF on" mode, plausibly suggesting that the SA release from the samples involves the interlayer intraparticle diffusion between the LDH layers (path I) and interparticle diffusion among the stacked SA-LDH shell nanocrystals (path II). The much lower R^2 values upon the Bhaskar model imply the interparticle diffusion among the magnetic particles (path III) is less important probably due to the larger space among the larger magnetic nanovehicle particles given their well dispersed morphology as shown in the SEM/TEM images. Additionally, for Fe_3O_4@SA-LDH-3.85, the Elovich model fits the release data under "no MF" mode better than the parabolic model, suggesting that the SA release from this sample is mainly determined by interlayer intraparticle diffusion between the LDH layers, while under "MF on" mode a little better Bhaskar fit ($R^2 > 0.91$) implies the slightly enhanced interparticle diffusion among the magnetic particles due to its slightly stronger magnetism. For Fe_3O_4@SA-LDH-1.93, the parabolic model better fits the release data under "no MF" mode, suggesting the SA release mainly by interparticle diffusion among the stacked SA-LDH nanocrystals (path II), in good agreement with its compact stack of LDH shell nanocrystals. Then, for Fe_3O_4@SA-LDH-7.71, both the parabolic and modified Freundlich models show better fits (R^2 in 0.95−0.99) under both "no MF" (a little better) and "MF on" modes, indicating that the SA release involves mainly the interlayer intraparticle diffusion among the LDH nanocrystals similar to the "floss-like" Fe_3O_4@SA-LDH-3.85 owing to their mainly vertically oriented LDH shell nanocrystals despite the former's cross-linking surfaces and coexistence with ZnO species as XPS shows.

Clearly, it can be conjectured that the SA release from Fe_3O_4@SA-LDH-1.93 with the LDH *ab*-face horizontal to the magnetite surface dominantly depends on path II, while those from magnetic nanovehicles with the LDH *ab*-face vertical to the magnetic surfaces mainly depend on path I. Briefly, the special and varied surface morphologies of Fe_3O_4@SA-LDH-*r* nanovehicles can effectively regulate the drug release process through modulating the dominating release path of SA from the series of magnetic nanovehicles. Figure 10 shows an illustration of the release mechanism for the hierarchical core@shell structural magnetic nanovehicles. The present Fe_3O_4@SA-

Table 1. Linear Correlation Coefficients (R^2) and Standard Deviation (SD) upon Several Kinetic Models Fitting to the Release Data

		Fe_3O_4@SA-LDH-1.93		Fe_3O_4@SA-LDH-3.85		Fe_3O_4@SA-LDH-7.71		SA-LDH
kinetic models	parameters	no MF	MF on	no MF	MF on	no MF	MF on	no MF
Elovich	R^2	0.9412	0.9657	0.9432	0.9611	0.9894	0.9527	0.9698
	SD	0.0220	0.0276	0.4837	0.0928	0.6410	0.4940	0.1874
parabolic diffusion	R^2	0.9703	0.9779	0.9414	0.9451	0.9561	0.9495	0.9138
	SD	0.0073	0.0039	0.0116	0.0369	0.0159	0.0130	0.0289
modified Freundlich	R^2	0.9110	0.9188	0.9198	0.9399	0.9868	0.9492	0.8515
	SD	0.0514	0.0619	0.0183	0.0689	0.0127	0.0139	0.1042
Bhaskar	R^2	0.8065	0.8366	0.9096	0.9112	0.9151	0.9286	0.7854
	SD	0.0045	0.0041	0.0411	0.0473	0.0412	0.0410	0.0593

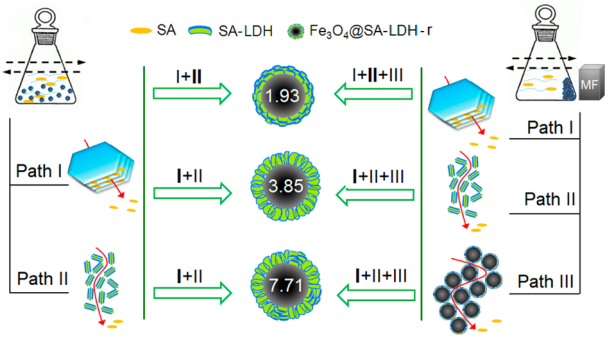

Figure 10. Schematic drawing of SA release from Fe_3O_4@SA-LDH-*r* with and without an external MF (bold number refers to the main release path).

LDH-*r* magnetic nanovehicles show a unique way for modulating the diffusion process of the SA guest, depending on the diversity of surface morphology. The magnetic nanovehicles are expected to be applied for the controlled drug release to meet a special requirement such as the targeted delivery of an antidote for the rapid cure of emergency symptoms.[60]

4. CONCLUSION

Novel organo-LDHs-based magnetic nanovehicles Fe_3O_4@SA-LDH-*r* were elaborately prepared via a double-drop coprecipitation strategy assembling salicylate intercalated ZnAl-LDH with varied growth orientations over the surface of the Fe_3O_4 submicrospheres of ca. 480 nm from aspirin and Zn- and Al-salts in a low supersaturation system with alkaline solutions. The obtained magnetic nanovehicles present hierarchical core@shell structure with a hexagonal LDH *ab*-face horizontal, vertical, and vertical/slant/horizontal to the Fe_3O_4 surface upon varied mass ratio (r = 1.93−7.71) of Zn-salt to Fe_3O_4 and possess moderate SA loadings and strong superparamagnetism. Fe_3O_4@SA-LDH-3.85 possesses a special "floss-like" morphology and the lowest shell compactness and thus the highest magnetic saturation. An *in vitro* release study indicates that under "no MF" mode the SA release exhibits the higher accumulated release percentage and the smaller half-life ($t_{0.5}$) for Fe_3O_4@SA-LDH-3.85 (41.2%, 1.63 min) and Fe_3O_4@SA-LDH-7.71 (51.1%, 1.66 min) probably owing to their largely vertical oriented LDH shell, while the dramatically reduced SA release (10.0%) and greatly elongated $t_{0.5}$ (25.6 min) for Fe_3O_4@SA-LDH-1.93 is probably due to its relatively stronger host−guest interaction and compact horizontally oriented LDH shell. Under "MF on" mode, all the magnetic nanovehicles exhibit a detectable slower SA release, which can be ascribed to the particle−particle interactions among the magnetic nanovehicles. The kinetic fittings indicate that the release behavior of all the samples involves the bulk and surface diffusion processes. Specially, the SA release from Fe_3O_4@SA-LDH-1.93 is mainly controlled by the interparticle diffusion among the horizontally packed LDH shell nanocrystals while those of Fe_3O_4@SA-LDH-3.85 and Fe_3O_4@SA-LDH-7.71 mainly involve the interlayer intraparticle diffusion between the LDHs layers. The obtained principles for morphology-controlled assembly of hierarchical core@shell structured organo-LDH magnetic nanovehicles could be extended to biological adsorption/separation, sustainable heterogeneous catalysis, and targeting drug delivery systems.

■ ASSOCIATED CONTENT

Supporting Information

FT-Raman spectra of SA-LDH, salicylic acid, and aspirin (Figure S1). Three-dimension model of SA obtained by Chemdraw Ultra 8.0 (Figure S2). SEM and TEM images of Fe_3O_4 nanoparticles (Figure S3). SEM image of pure SA-LDH (Figure S4). EDX mapping analysis of Fe_3O_4@SA-LDH-3.85 (Figure S5). pH of Fe_3O_4 aqueous suspension as a function concentration of the total H^+ ions added to the system (H_t) (Figure S6). Gran functions (G) for the Fe_3O_4 sample (Figure S7 attached the determination of surface OH site density (D_s) of Fe_3O_4 sample). SEM images of Fe_3O_4@LA-ZnAl-LDH and Fe_3O_4@SA-MgAl-LDH (Figure S8 attached with the synthesis experiment). TG-DTA curves of pure SA and SA-LDH (Figure S9). FT-IR spectra of Fe_3O_4@SA-LDH-3.85 before and after the *in vitro* drug release test (Figure S10). *In vitro* release profiles of SA-LDH and Fe_3O_4@SA-LDH-*r* in pH 4.60 PBS (Figure S11). XRD structural parameters and chemical compositions of the Fe_3O_4@SA-LDH-*r* magnetic nanovehicles and related samples (Table S1). XPS results of the Fe_3O_4@SA-LDH-*r* magnetic nanovehicles and related samples (Table S2). The ion products and coprecipitation pH values in the synthesis process of varied LDH systems (Table S3). Kinetic parameters about the homogeneous nucleation process of $Zn(OH)_2$ and $Mg(OH)_2$ (Table S4). This material is available free of charge via the Internet at http://pubs.acs.org.

■ AUTHOR INFORMATION

Corresponding Author

*E-mail: huizhang67@gst21.com. Tel: +8610-6442 5872. Fax: +8610-6442 5385.

Notes

The authors declare no competing financial interest.

■ ACKNOWLEDGMENTS

The authors greatly appreciate the financial support by the National Basic Research Program of China (2011CBA00508) and the National Nature Science Foundation of China (21276015).

■ REFERENCES

(1) Li, F.; Duan, X. Applications of Layered Double Hydroxides. In *Layered Double Hydroxides, Structure and Bonding*; Duan, X., Evans, D. G., Eds.; Springer: Berlin/Heidelberg, 2006; Vol. *119*, pp 193−223.

(2) Sideris, P. J.; Nielsen, U. G.; Gan, Z. H.; Grey, C. P. Mg/Al Ordering in Layered Double Hydroxides Revealed by Multinuclear NMR Spectroscopy. *Science* **2008**, *321*, 113−117.

(3) He, S.; An, Z.; Wei, M.; Evans, D. G.; Duan, X. Layered Double Hydroxide-Based Catalysts: Nanostructure Design and Catalytic Performance. *Chem. Commun.* **2013**, *49*, 5912−5920.

(4) Goh, K.-H.; Lim, T.-T.; Dong, Z. Application of Layered Double Hydroxides for Removal of Oxyanions: A Review. *Water Res.* **2008**, *42*, 1343−1368.

(5) Ruiz-Hitzky, E.; Aranda, P.; Darder, M.; Rytwo, G. Hybrid Materials Based on Clays for Environmental and Biomedical Applications. *J. Mater. Chem.* **2010**, *20*, 9306−9321.

(6) Khan, A. I.; Ragavan, A.; Fong, B.; Markland, C.; O'Brien, M.; Dunbar, T. G.; Williams, G. R.; O'Hare, D. Recent Developments in the Use of Layered Double Hydroxides as Host Materials for the Storage and Triggered Release of Functional Anions. *Ind. Eng. Chem. Res.* **2009**, *48*, 10196−10205.

(7) Choy, J.-H.; Kwak, S.-Y.; Jeong, Y.-J.; Park, J.-S. Inorganic Layered Double Hydroxides as Nonviral Vectors. *Angew. Chem., Int. Ed.* **2000**, *39*, 4041−4045.

(8) Ladewig, K.; Xu, Z. P.; Lu, G. Q. Layered Double Hydroxide Nanoparticles in Gene and Drug Delivery. *Expert Opin. Drug Delivery* **2009**, *6*, 907−922.
(9) Huang, W.; Zhang, H.; Pan, D. K. Study on the Release Behavior and Mechanism by Monitoring the Morphology Changes of the Large-Sized Drug-LDH Nanohybrids. *AIChE J.* **2011**, *57*, 1936−1946.
(10) Choi, S.-J.; Choy, J.-H. Layered Double Hydroxide Nanoparticles as Target-Specific Delivery Carriers: Uptake Mechanism and Toxicity. *Nanomedicine* **2011**, *6*, 803−814.
(11) Zhang, H.; Zou, K.; Guo, S. H.; Duan, X. Nanostructural Drug-Inorganic Clay Composites: Structure, Thermal Property and *In Vitro* Release of Captopril-Intercalated Mg-Al-Layered Double Hydroxides. *J. Solid State Chem.* **2006**, *179*, 1791−1800.
(12) Rives, V.; Del Arco, M.; Martín, C. Layered Double Hydroxides as Drug Carriers and for Controlled Release of Non-Steroidal Antiinflammatory Drugs (NSAIDs): A Review. *J. Controlled Release* **2013**, *169*, 28−39.
(13) Riaz, U.; Ashraf, S. M. Double Layered Hydroxides as Potential Anti-Cancer Drug Delivery Agents. *Mini-Rev. Med. Chem.* **2013**, *13*, 522−529.
(14) Chomoucka, J.; Drbohlavova, J.; Huska, D.; Adam, V.; Kizek, R.; Hubalek, J. Magnetic Nanoparticles and Targeted Drug Delivering. *Pharmacol. Res.* **2010**, *62*, 144−149.
(15) Dilnawaz, F.; Singh, A.; Mohanty, C.; Sahoo, S. K. Dual Drug Loaded Superparamagnetic Iron Oxide Nanoparticles for Targeted Cancer Therapy. *Biomaterials* **2010**, *31*, 3694−3706.
(16) Chaudhuri, R. G.; Paria, S. Core/Shell Nanoparticles: Classes, Properties, Synthesis Mechanisms, Characterization, and Applications. *Chem. Rev.* **2012**, *112*, 2373−2433.
(17) Hayashi, K.; Ono, K.; Suzuki, H.; Sawada, M.; Moriya, M.; Sakamoto, W.; Yogo, T. High-Frequency, Magnetic-Field-Responsive Drug Release from Magnetic Nanoparticle/Organic Hybrid Based on Hyperthermic Effect. *ACS Appl. Mater. Interfaces* **2010**, *2*, 1903−1911.
(18) Zhao, W. R.; Gu, J. L.; Zhang, L. X.; Chen, H. R.; Shi, J. L. Fabrication of Uniform Magnetic Nanocomposite Spheres with a Magnetic Core/Mesoporous Silica Shell Structure. *J. Am. Chem. Soc.* **2005**, *127*, 8916−8917.
(19) Chen, L. L.; Li, L.; Zhang, L. Y.; Xing, S. X.; Wang, T. T.; Wang, Y. A.; Wang, C. G.; Su, Z. M. Designed Fabrication of Unique Eccentric Mesoporous Silica Nanocluster-Based Core-Shell Nanostructures for pH-Responsive Drug Delivery. *ACS Appl. Mater. Interfaces* **2013**, *5*, 7282−7290.
(20) Zhang, H.; Zou, K.; Sun, H.; Duan, X. A Magnetic Organic-Inorganic Composite: Synthesis and Characterization of Magnetic 5-Aminosalicylic Acid Intercalated Layered Double Hydroxides. *J. Solid State Chem.* **2005**, *178*, 3485−3493.
(21) Carja, G.; Chiriac, H.; Lupu, N. New Magnetic Organic-Inorganic Composites Based on Hydrotalcite-Like Anionic Clays for Drug Delivery. *J. Magn. Magn. Mater.* **2007**, *311*, 26−30.
(22) Zhang, H.; Pan, D. K.; Duan, X. Synthesis, Characterization, and Magnetically Controlled Release Behavior of Novel Core-Shell Structural Magnetic Ibuprofen-Intercalated LDH Nanohybrids. *J. Phys. Chem. C* **2009**, *113*, 12140−12148.
(23) Zhang, H.; Pan, D. K.; Zou, K.; He, J.; Duan, X. A Novel Core-Shell Structured Magnetic Organic-Inorganic Nanohybrid Involving Drug-Intercalated Layered Double Hydroxides Coated on a Magnesium Ferrite Core for Magnetically Controlled Drug Release. *J. Mater. Chem.* **2009**, *19*, 3069−3077.
(24) Pan, D. K.; Zhang, H.; Fan, T.; Chen, J. G.; Duan, X. Nearly Monodispersed Core-Shell Structural Fe_3O_4@DFUR-LDH Submicro Particles for Magnetically Controlled Drug Delivery and Release. *Chem. Commun.* **2011**, *47*, 908−910.
(25) Ay, A. N.; Konuk, D.; Zümreoğlu-Karan, B. Magnetic Nanocomposites with Drug-Intercalated Layered Double Hydroxide Shell Supported on Commercial Magnetite and Laboratory-Made Magnesium Ferrite Core Materials. *Mater. Sci. Eng., C* **2011**, *31*, 851−857.
(26) Mi, F.; Chen, X. T.; Ma, Y. W.; Yin, S. T.; Yuan, F. L.; Zhang, H. Facile Synthesis of Hierarchical Core-Shell Fe_3O_4@MgAl-LDH@Au as Magnetically Recyclable Catalysts for Catalytic Oxidation of Alcohols. *Chem. Commun.* **2011**, *47*, 12804−12806.
(27) Chen, X. T.; Mi, F.; Zhang, H.; Zhang, H. Q. Facile Synthesis of a Novel Magnetic Core-Shell Hierarchical Composite Submicrospheres Fe_3O_4@CuNiAl-LDH under Ambient Conditions. *Mater. Lett.* **2012**, *69*, 48−51.
(28) Zhang, H.; Zhang, G. Y.; Bi, X.; Chen, X. T. Facile Assembly of a Hierarchical Core@Shell Fe_3O_4@CuMgAl-LDH (Layered Double Hydroxide) Magnetic Nanocatalyst for the Hydroxylation of Phenol. *J. Mater. Chem. A* **2013**, *1*, 5934−5942.
(29) Shao, M. F.; Ning, F. Y.; Zhao, J. W.; Wei, M.; Evans, S. G.; Duan, X. Preparation of Fe_3O_4@SiO_2@Layered Double Hydroxide Core-Shell Microspheres for Magnetic Separation of Proteins. *J. Am. Chem. Soc.* **2012**, *134*, 1071−1077.
(30) Fan, T.; Pan, D. K.; Zhang, H. Study on Formation Mechanism by Monitoring the Morphology and Structure Evolution of Nearly Monodispersed Fe_3O_4 Submicroparticles with Controlled Particle Sizes. *Ind. Eng. Chem. Res.* **2011**, *50*, 9009−9018.
(31) Hawley, S. A.; Fullerton, M. D.; Ross, F. A.; Schertzer, J. D.; Chevtzoff, C.; Walker, K. J.; Peggie, M. W.; Zibrova, D.; Green, K. A.; Mustard, K. J.; Kemp, B. E.; Sakamoto, K.; Steinberg, G. R.; Hardie, D. G. The Ancient Drug Salicylate Directly Activates AMP-Activated Protein Kinase. *Science* **2012**, *36*, 918−922.
(32) Reynolds, E. F., Ed. *Aspirin and Similar Analgesic and Anti-Inflammatory Agents, Martindale — the Extra Pharmacopoeia*, 28th ed.; Pharmaceutical Press: London, 1982; pp 234.
(33) Yang, J.-H.; Han, Y.-S.; Park, M.; Park, T.; Hwang, S.-J.; Choy, J.-H. New Inorganic-Based Drug Delivery System of Indole-3-Acetic Acid-Layered Metal Hydroxide Nanohybrids with Controlled Release Rate. *Chem. Mater.* **2007**, *19*, 2679−2685.
(34) Gu, Z.; Thomas, A. C.; Xu, Z. P.; Campbell, J. H.; Lu, G. Q. *In Vitro* Sustained Release of LMWH from MgAl-Layered Double Hydroxide Nanohybrids. *Chem. Mater.* **2008**, *20*, 3715−3722.
(35) Ge, J. P.; Hu, Y. X.; Biasini, M.; Beyermann, W. P.; Yin, Y. D. Superparamagnetic Magnetite Colloidal Nanocrystal Clusters. *Angew. Chem., Int. Ed.* **2007**, *46*, 4342−4345.
(36) Del Arco, M.; Gutiérrez, S.; Martín, C.; Rives, V.; Rocha, J. Synthesis and Characterization of Layered Double Hydroxides (LDH) Intercalated with Non-Steroidal Anti-Inflammatory Drugs (NSAID). *J. Solid State Chem.* **2004**, *177*, 3954−3962.
(37) Nakamoto, K. *Infrared and Raman Spectra of Inorganic and Coodination Compounds*, 6th ed; Wiley: New York, 1997.
(38) Zou, K.; Zhang, H.; Duan, X. Studies on the Formation of 5-Aminosalicylate Intercalated Zn-Al Layered Double Hydroxides as a Function of Zn/Al Molar Ratios and Synthesis Routes. *Chem. Eng. Sci.* **2007**, *62*, 2022−2031.
(39) Lewandowski, W.; Kalinowska, M.; Lewandowska, H. The Influence of Metals on the Electronic System of Biologically Important Ligands. Spectroscopic Study of Benzoates, Salicylates, Nicotinates and Isoorotates. Review. *J. Inorg. Biochem.* **2005**, *99*, 1407−1423.
(40) Krishnakumar, V.; Mathammal, R. Density Functional and Experimental Studies on the FT-IR and FT-Raman Spectra and Structure of Benzoic Acid and 3,5-Dichlro Salicylic Acid. *J. Raman Spectrosc.* **2009**, *40*, 264−271.
(41) Varghese, H. T.; Panicker, C. Y.; Philip, D.; Mannekutla, J. R.; Inamdar, S. R. IR, Raman and SERS Studies of Methyl Salicylate. *Spectrochim. Acta, Part A* **2007**, *66*, 959−963.
(42) Ji, J. G.; Hao, S. L.; Wu, D. J.; Huang, R.; Xu, Y. Preparation, Characterization and *In Vitro* Release of Chitosan Nanoparticles Loaded with Gentamicin and Salicylic Acid. *Carbohydr. Polym.* **2011**, *85*, 803−808.
(43) Cao, S. Q.; Fu, X. J.; Wang, N. X.; Wang, H.; Yang, Y. J. Release Behavior of Salicylic Acid in Supramolecular Hydrogels Formed by L-Phenylalanine Derivatives as Hydrogelator. *Int. J. Pharm. (Amsterdam, Neth.)* **2008**, *357*, 95−99.
(44) Bonina, F. P.; Giannossi, M. L.; Medici, L.; Puglia, C.; Summa, V.; Tateo, F. Adsorption of Salicylic Acid on Bentonite and Kaolin and Release Experiments. *Appl. Clay Sci.* **2007**, *36*, 77−85.

(45) Hong, J. H.; Wang, Y. F.; He, G.; Wang, J. X. The Effect of Calcination Temperature on the Photoluminescence from Sol-Gel Derived Amorphous ZnO/Silica Composites. *J. Non-Cryst. Solids* **2010**, *356*, 2778−2780.
(46) Fleutot, S.; Dupin, J.-C.; Renaudin, G.; Martinez, H. Intercalation and Grafting of Benzene Derivatives into Zinc-Aluminum and Copper-Chromium Layered Double Hydroxide Hosts: An XPS Monitoring Study. *Phys. Chem. Chem. Phys.* **2011**, *13*, 17564−17578.
(47) Kinniburgh, D. G.; Jackson, M. L. Cation Adsorption by Hydrous Metal Oxides and Clay. In *Adsorption of Inorganics at Solid-Liquid Interfaces*; Anderson, M. A., Rubin, A. J., Eds.; Ann Arbor Science Publisher: Ann Arbor, MI, 1981; pp 91−160.
(48) Jaubertie, C.; Holgado, M. J.; San Román, M. S.; Rives, V. Structural Characterization and Delamination of Lactate-Intercalated Zn, Al-Layered Double Hydroxides. *Chem. Mater.* **2006**, *18*, 3114−3121.
(49) Prevot, V.; Forano, C.; Besse, J. P. Syntheses and Thermal and Chemical Behaviors of Tartrate and Succinate Intercalated Zn_3Al and Zn_2Cr Layered Double Hydroxides. *Inorg. Chem.* **1998**, *37*, 4293−4301.
(50) Kashchiev, D.; van Rosmalen, G. M. Review: Nucleation in Solution Revisited. *Cryst. Res. Technol.* **2003**, *38*, 555−574.
(51) Adachi-Pagano, M.; Forano, C.; Besse, J. P. Synthesis of Al-Rich Hydrotalcite-Like Compounds by Using the Urea Hydrolysis Reaction-Control of Size and Morphology. *J. Mater. Chem.* **2003**, *13*, 1988−1993.
(52) Yang, X. F.; Sun, Z. X.; Wang, D. S.; Forsling, W. Surface Acid-Base Properties and Hydration/Dehydration Mechanisms of Aluminum (Hydr)Oxides. *J. Colloid Interface Sci.* **2007**, *308*, 395−404.
(53) Tsyganenko, A. A.; Filimonov, V. N. Infrared Spectra of Surface Hydroxyl Groups and Crystallites Structure of Oxides. *J. Mol. Struct.* **1973**, *19*, 579−589.
(54) Huang, C.-P.; Stumm, W. Specific Adsorption of Cations on Hydrous γ-Al_2O_3. *J. Colloid Interface Sci.* **1973**, *42*, 409−420.
(55) McBride, M. B. *Environmental Chemistry of Soils*; Oxford Univ. Press: New York, 1994; pp 121.
(56) Lu, J.; Jiao, X. L.; Chen, D. R.; Li, W. Solvothermal Synthesis and Characterization of Fe_3O_4 and γ-Fe_2O_3 Nanoplates. *J. Phys. Chem. C* **2009**, *113*, 4012−4017.
(57) Cullity, B. D. *Introduction to Magnetic Materials*; Addison-Wesley: Reading, MA; London, 1972; pp 190.
(58) He, H. M.; Kang, H. L.; Ma, S. L.; Bai, Y. X.; Yang, X. J. High Adsorption Selectivity of ZnAl Layered Double Hydroxides and the Calcined Materials toward Phosphate. *J. Colloid Interface Sci.* **2010**, *343*, 225−231.
(59) Costantino, U.; Casciola, M.; Massinelli, L.; Nocchetti, M.; Vivani, R. Intercalation and Grafting of Hydrogen Phosphates and Phosphonates into Synthetic Hydrotalictes and a.c.-Conductivity of the Compounds Thereby Obtained. *Solid State Ionics* **1997**, *97*, 203−212.
(60) Elzoghby, A. O.; Samy, W. M.; Elgindy, N. A. Albumin-Based Nanoparticles as Potential Controlled Release Drug Delivery Systems. *J. Controlled Release* **2012**, *157*, 168−182.